iScience

CellPress
OPEN ACCESS

Article

Composition effects of electrodeposited Cu-Ag nanostructured electrocatalysts for CO_2 reduction

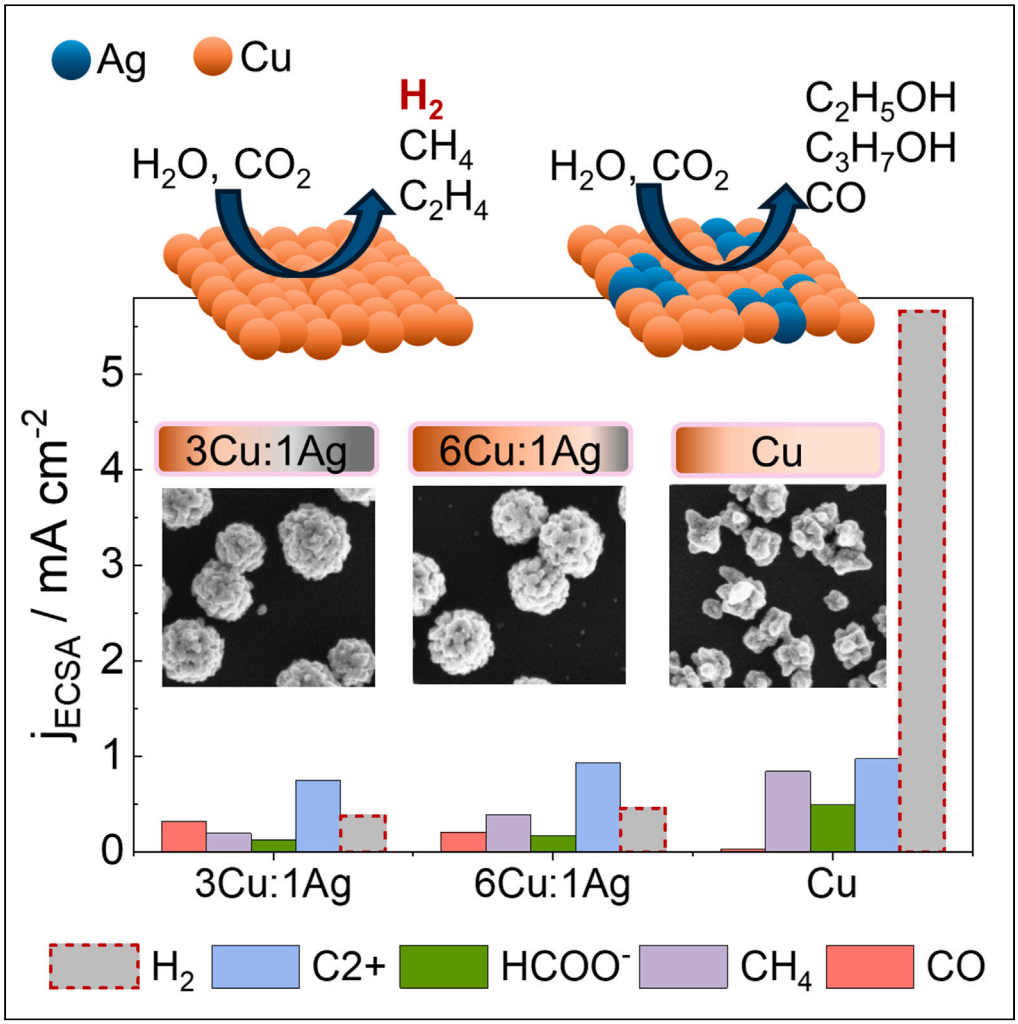

Elena Plaza-Mayoral, Valery Okatenko, Kim N. Dalby, Hanne Falsig, Ib Chorkendorff, Paula Sebastián-Pascual, María Escudero-Escribano

paula.pascual@chem.ku.dk (P.S.-P.)
maria.escudero@icn2.cat (M.E.-E.)

Highlights

Cu-Ag nanocatalysts have been electrodeposited in a choline chloride urea DES

We use voltammetric lead UPD to determine the ECSA and intrinsic catalytic performance

The addition of silver to copper highly suppresses the hydrogen formation

Silver increases the formation of liquid products over ethylene on copper

Plaza-Mayoral et al., iScience *27*, 109933
June 21, 2024
https://doi.org/10.1016/j.isci.2024.109933

iScience

CellPress
OPEN ACCESS

Article

Composition effects of electrodeposited Cu-Ag nanostructured electrocatalysts for CO_2 reduction

Elena Plaza-Mayoral,[1] Valery Okatenko,[2] Kim N. Dalby,[3] Hanne Falsig,[3] Ib Chorkendorff,[4] Paula Sebastián-Pascual,[1,*] and María Escudero-Escribano[1,5,6,7,*]

SUMMARY

The electrochemical carbon dioxide reduction (CO_2RR) on Cu-based catalysts is a promising strategy to store renewable electricity and produce valuable C_{2+} chemicals. We investigate the CO_2RR on Cu-Ag nanostructures that have been electrodeposited in a green choline chloride and urea deep eutectic solvent (DES). We determine the electrochemically active surface area (ECSA) using lead underpotential deposition (UPD) to investigate the CO_2RR intrinsic activity and selectivity. We show that the addition of Ag on electrodeposited Cu primarily suppresses the production of hydrogen and methane. While the production of carbon monoxide slightly increases, the partial current of the total C_{2+} products does not considerably increase. Despite that the production rate of C_{2+} is similar on Cu and Cu-Ag, the addition of Ag enhances the formation of alcohols and oxygenates over ethylene. We highlight the potential of metal electrodeposition from DES as a sustainable strategy to develop bimetallic Cu-based nanocatalysts for CO_2RR.

INTRODUCTION

To reduce the negative effect of greenhouse gas emissions such as carbon dioxide, a broad range of mitigation strategies coupled with renewable energy have been intensively investigated in the last decade.[1] The electrochemical reduction of carbon dioxide (CO_2RR) is a long-term solution to produce renewable chemicals and fuels and close the unbalanced carbon cycle.[2–6] In particular, the design of new catalyst structures to convert CO_2 molecules into renewable liquid fuels such as ethanol and propanol has gained increasing interest. These green fuels are compatible with current energy infrastructure, can be used in transportation, and are easily and safely stored and transported.[7–12] Moreover, the CO_2RR also produces other minor products, such as acetate, acetaldehyde, or ethylene glycol, which are building block molecules used in industry to produce further long-chain carboxylates or bio-based chemicals.[13–18]

Copper and Cu-based materials have been the most investigated metallic electrocatalysts for the CO_2RR as they can reduce CO_2 beyond CO and HCOOH and produce valuable multi-carbon products.[7,19,20] Even though pure copper is capable of converting CO_2 to C_{2+} products with relatively high activities, the reaction is still limited due to the competing hydrogen evolution reaction (HER) and the low product selectivity. The reduction of CO_2 to C_{2+} products on copper is mainly limited to ethylene (C_2H_4), whereas other C_2 or C_3 products such as ethanol and propanol are often generated in lower amounts.[21] The formation of ethylene and ethanol occurs via a C-C coupling reaction of two adsorbed CO molecules which leads to a common hydrogenated dimer intermediate.[9] This intermediate first evolves into ethylene and then is converted into ethanol after subsequent hydrogenation steps, or to propanol if a third CO molecule is inserted.[22] As the number of electrons required to produce alcohols on copper is higher than to produce ethylene, ethylene is generally favored on copper except on some specific surface structures or single facets.[14,23–25]

Different strategies and types of copper-based surfaces with tailored structure and composition have been prepared aiming to switch selectivity toward oxygenates and alcohols over ethylene. The first strategy relies on tuning the surface structure or the shape and size of the nanoparticles (NPs). Copper nanocubes of 44 nm with more (110)/(100) steps edges were found to favor the C-C coupling, enhancing the selectivity toward C_2H_4 up to 40% and over 10% of C_2H_6O and C_3H_8O.[26] Recently, Aran-Ais et al. have also shown how applying pulses to Cu(100) changes the surface structure, increasing the production of ethanol to near 30%, similar to the Cu(310) facet reported by Hori and

[1]Center for High Entropy Alloy Catalysis, Department of Chemistry, University of Copenhagen, Universitetsparken 5, 2100 Copenhagen, Denmark
[2]Laboratory of Nanochemistry for Energy Research, Institute of Chemical Sciences and Engineering, Ecole Polytechnique Fédérale de Lausanne, CH-1950 Sion, Switzerland
[3]Topsoe A/S, Haldor Topsøe Allé 1, DK-2800 Kgs, Lyngby, Denmark
[4]Department of Physics, Surface Physics and Catalysis, Technical University of Denmark, Fysikvej, DK-2800 Lyngby, Denmark
[5]Catalan Institute of Nanoscience and Nanotechnology (ICN2), CSIC, Barcelona Institute of Science and Technology, UAB, 08193 Bellaterra, Barcelona, Spain
[6]Catalan Institution for Research and Advanced Studies (ICREA), Pg. Lluís Companys 23, 08010 Barcelona, Spain
[7]Lead contact
*Correspondence: paula.pascual@chem.ku.dk (P.S.-P.), maria.escudero@icn2.cat (M.E.-E.)
https://doi.org/10.1016/j.isci.2024.109933

co-workers.[27,28] Another strategy is based on tandem catalysts, i.e., the reaction occurs in two steps catalyzed by two different metals.[19,29,30] Jaramillo et al. presented a tandem catalyst of Au NPs on a polycrystalline Cu foil, in which gold increased the CO concentration on the surrounding copper, where the CO was selectively reduced to alcohols.[29] Finally, tuning the electronic structure by metal alloying allows to favor alcohol production over C_2H_4, e.g., by combining Cu with Zn, Pd, or Ag.[31–34] In particular, Cu-Ag are promising bimetallic catalysts to reduce CO_2 to liquid and oxygenated products such as ethanol, propanol, acetaldehyde, and ethylene glycol as both tandem catalysts and alloys.[30,35–37]

On one side, pure Ag electrocatalysts are typically selective toward CO production under CO_2RR conditions.[38] Previous studies have shown how mixing Cu and Ag enhances the production of C_{2+} products by increasing the CO coverage on the surface or by blocking specific sites that might produce the competing H_2 instead.[30,39,40] A study on copper-silver composites suggested that the CO availability is key to enhance the ethanol production, either by *CO dimerization or via an alternative open pathway of *CO and *CH_x coupling.[37] Cu-Ag tandem catalysts also confirmed facet-dependent production of ethanol via *CO - *CH_x coupling at edges and corner sites adjacent to Ag atoms because of the *CO enrichment on the surface.[30] On the other hand, a study on Cu-Ag surface alloys presented the formation of multi-carbon oxygenates due to compressive surface strain of the Cu atoms which selectively suppresses the HER by weakening the adsorption energy of *H.[39] On a similar basis, through a compressive strain and reduced electron density, Cu-Ag multi-phase alloys were also proved to be promising catalysts for the production of acetaldehyde.[36]

These Cu-Ag catalysts for CO_2RR have been prepared through different chemical and physical synthesis methods over the years.[39,41] Colloidal synthesis has been widely employed for the preparation of NPs followed by their deposition onto the chosen substrate.[30,42] However, they usually need surfactant agents or additives to control the growth of the NPs, which might adhere on the surface inhibiting the electrocatalytic response, meaning that they need to be removed in subsequent time and energy-consuming cleaning steps.[43] Co-sputtering of the metals allows for the preparation of surfaces with controlled composition and has been further scaled, although it requires the use of ultra-high vacuum which consumes a high amount of energy.[9] Metal electrodeposition in green non-aqueous solvents has emerged as an easy alternative for the preparation of new bi- and multi-metallic nanostructures.[44,45] Electrodeposition is a versatile and affordable technique widely employed in the plating industry to prepare a broad range of materials such as metallic NPs and thin films, metal oxides, composites, and alloys.[46] Metal electrodeposition in deep eutectic solvents (DESs) offers several advantages in contrast to aqueous media. DESs present a wider electrochemical window, good conductivity, and good stability, they do not require the addition of any surfactants for a controllable deposition, and they are soluble in water, non-toxic, and facilitate the preparation of deposits with a homogeneous distribution over the substrate surface.[45,47–51]

In this paper, we use a sustainable and simple method to prepare electrodeposited Cu-Ag bimetallic nanostructured catalysts from a choline chloride urea DES and for CO_2RR.[52] We have prepared Cu and Cu-Ag nanostructures and rationally assessed how the introduction of silver changes the product selectivity and intrinsic activity toward CO_2RR. We have used two different bath compositions and prepared different loadings to evaluate how small changes in surface morphology, size of the nanostructures, and composition affect the performance. We have evaluated our nanocatalysts for the CO_2RR at different potentials in terms of product selectivity. We have addressed how different Ag/Cu ratios influence the production of oxygenates over ethylene, as well as the formation of hydrogen in the competing HER reaction of our electrodeposited Cu-Ag nanostructures. Finally, although Cu-Ag produces valuable oxygenated compounds, selectivity varies significantly between different reports, likely due to the sensitivity of the reaction to composition, size, or morphology of the catalyst.[39] In this regard, we want to highlight the importance of estimating the electrochemically active surface area (ECSA) to separate the effects of having different structures and large areas in NPs and nanostructures from their intrinsic catalytic performance.[7]

The intrinsic activity refers to the current densities normalized by the number of actives sites or ECSA. Typically, electrochemical methods such as capacitance measurements are used to address the ECSA. Capacitance measurements calculate the double-layer capacitance in the potential window of the electrode where no faradaic process occurs. Then, this capacitance value is normalized by the capacitance of the corresponding flat surface which requires knowing the capacitance value of the bimetallic phase. Capacitance measurements provide very small currents which can significantly vary with the presence of contaminants in solution or adsorption processes such as the reduction of oxygen traces, making it difficult to estimate the ECSA.[53,54] Alternatively, physical methods such as the Brunauer-Emmett-Teller (BET) isotherm can be used to assess the specific surface area of a broad range of materials such as powders, oxides, nanostructures, and porous materials. The BET isotherm determines the surface area by monitoring the adsorption of a monolayer of molecules from a gas phase, such as nitrogen, onto the catalyst surface.[55] We have recently shown that one valuable method to estimate the ECSA of copper and copper-based catalysts is to record the voltammetric lead underpotential deposition (UPD) on copper.[56] Metal underpotential deposition is a surface structure-sensitive process and provides direct information on the surface state and number of surface sites available for the reaction. Lead UPD provides intense and reversible features that correspond to the reversible adsorption/desorption of a sub-monolayer of lead on copper and silver, thus providing quantitative information on the number of surface active sites per unit area.[57,58] Thus, we have determined the ECSA by using lead UPD to rationally address how the addition of different amounts of silver modifies the intrinsic partial currents of the products formed during the CO_2 conversion.

RESULTS

To assess how the Cu/Ag ratio in the nanostructures affects the CO_2RR, we electrodeposited bimetallic nanostructured electrocatalysts with tunable composition by using two different bath compositions: 0.075 M $CuCl_2$/0.025 M AgCl + DES solution and 0.081 M $CuCl_2$/0.014 M AgCl + DES solution (Figure S1). We named the nanostructures prepared from these solutions as 3Cu:1Ag and 6Cu:1Ag, respectively, in which

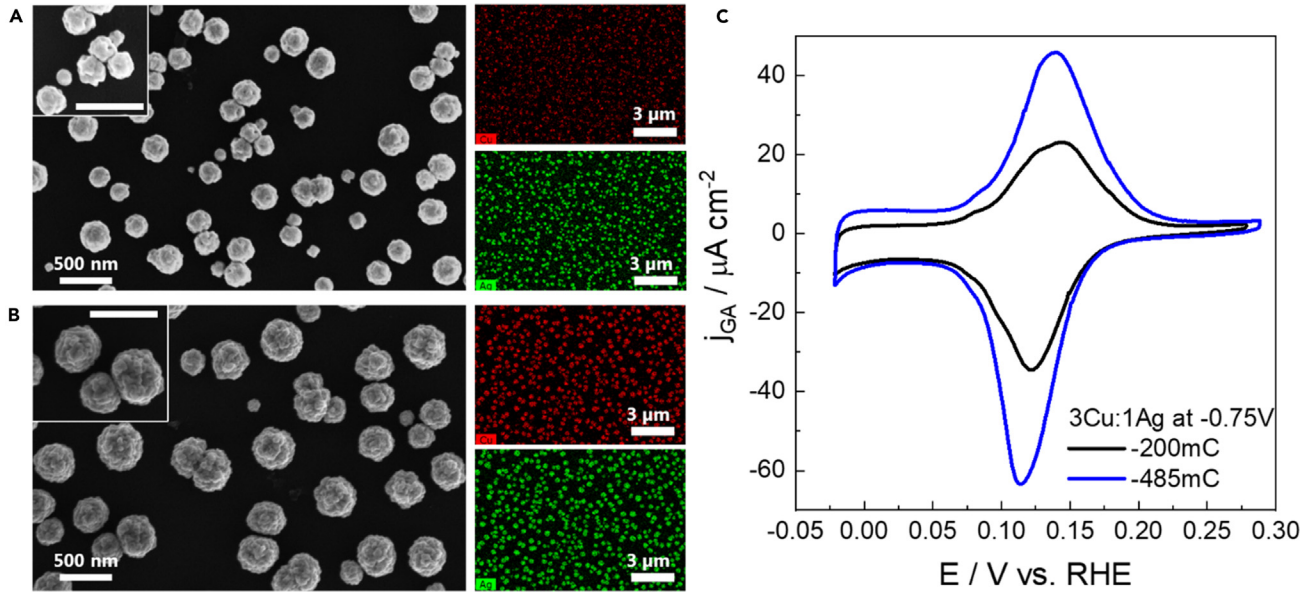

Figure 1. Characterization of the Cu-Ag nanostructures morphology with SEM and determination of the ECSA before reaction

(A and B) (A) SEM of 3Cu:1Ag at −0.65 $V_{Ag|AgCl}$ and −200 mC, and (B) SEM of the same sample at −485 mC with the corresponding EDS maps. The scale bars on the inlet SEM images correspond to 500 nm.

(C) Lead UPD of the nanostructures at (A) and (B). The pH of the Pb UPD electrolyte is 3.2.

the number indicates the 3:1 and 6:1 M ratio from the bath solution of Cu and Ag, respectively. Pure Cu nanostructures were also prepared from a 0.1 M $CuCl_2$ + DES solution and compared with the Cu-Ag nanostructures. We have characterized our systems by cyclic voltammetry and chronoamperometry (CA) to evaluate the optimal potential range to perform the electrodeposition on a glassy carbon. In this range, the current-time CA transients exhibit the characteristic shape of a nucleation and growth mechanism (Figure S2A and S2B).[49,56,59] We prepared the deposit at moderate rates by applying a moderate applied overpotential in between the optimal range. For the Cu-Ag systems, at electrodeposition applied potentials between −0.65 $V_{Ag|AgCl}$ and −0.75 $V_{Ag|AgCl}$, we obtain a homogeneous and stable surface, whereas higher applied overpotentials lead to poorly adherent deposits. A detailed description of the electrochemical characterization is explained in the Supplemental Information (S.I). The 3Cu:1Ag deposits were prepared at a potential of −0.65 $V_{Ag|AgCl}$, the 6Cu:1Ag deposit at a potential of −0.68 $V_{Ag|AgCl}$, and the single Cu deposits at a potential of −1.05 $V_{Ag|AgCl}$. At these applied potentials, solvent co-reduction does not overlap with the metal electrodeposition. Therefore, we have assumed that the electrodeposition has an efficiency of 100% and all the circulated charge is related to the reduction of the metal ions in solution.

We electrodeposited nanostructures with three different loadings by controlling the time of deposition and circulated charge, aiming to address how the loading influences the morphology, size, and composition of the nanostructures. We deposited nanostructures on the glassy carbon with 5.29 cm^2 area using three circulated charges: Q = −200, −270, and −485 mC. Then we characterized the Cu-Ag nanostructures using SEM (Figures S3, S4 and S5), X-ray photoelectron spectroscopy (XPS) (Figures S6 and S7), and energy-dispersive X-ray spectroscopy (EDS). Figures 1A and 1B illustrate the characterization of 3Cu:1Ag at −200 and −485 mC, respectively. We observed rounded and rough Cu-Ag NPs. Figure S3 also shows higher-resolution SEM images of the three loadings in which we can relate the roughness with visible porosity. At high coverages, the NPs become slightly bigger (from 200 up to 400 nm) likely due to surface diffusion and progressive electrodeposition. The XPS spectrum of the 3Cu:1Ag sample at −485 mC (Figure S7A and S7B) shows that the surface composition is 1:1 after applying 20 s of sputtering to remove any traces of contamination. The main Cu2p region has split spin-orbit components with a 20-eV separation: $Cu2p_{1/2}$ and $Cu2p_{3/2}$. The 3Cu:1Ag exhibits these peaks centered at 932.7 and 933.5 eV, close to their observable values at 932.5–933 eV. Cu2p spectra are usually accompanied by characteristic satellites that will help to distinguish the copper oxidation states. We attribute the Cu2p peaks in both samples to metallic copper and Cu_2O since no strong double satellite peaks have been identified but only weak satellites c.a. 945 eV characteristic from Cu(I), as observed in Figures S7A.[60–63] Figure S7B illustrates the spectrum of the Ag3d region which is characterized by well-separated spin-orbit components: $Ag3d_{3/2}$ and $Ag3d_{5/2}$. Both components of the metallic silver spectra are usually accompanied by loss features at higher binding energies. These specific energy losses are related to silver plasmon losses which are not subtracted with the Shirley background.[64,65] The main $Ag3d_{5/2}$ is centered at 368.6 eV close to the known binding energy of 368.2 eV[60,61] We have determined a Cu/Ag weight surface relationship of 1:1 for the 3Cu:1Ag sample.

The EDS color maps show how both metals are distributed all over the substrate with a bulk composition of 1.8:1 of Cu and Ag. We have calculated the mass loadings based on the EDS results using Faraday's law and have obtained a mass loading of 0.1 mg for −200 mC, 0.14 mg for −270 mC, and 0.24 mg for −485 mC, which equals 19, 26, and 45 μg cm^{-2}, respectively. The EDS results have confirmed that the

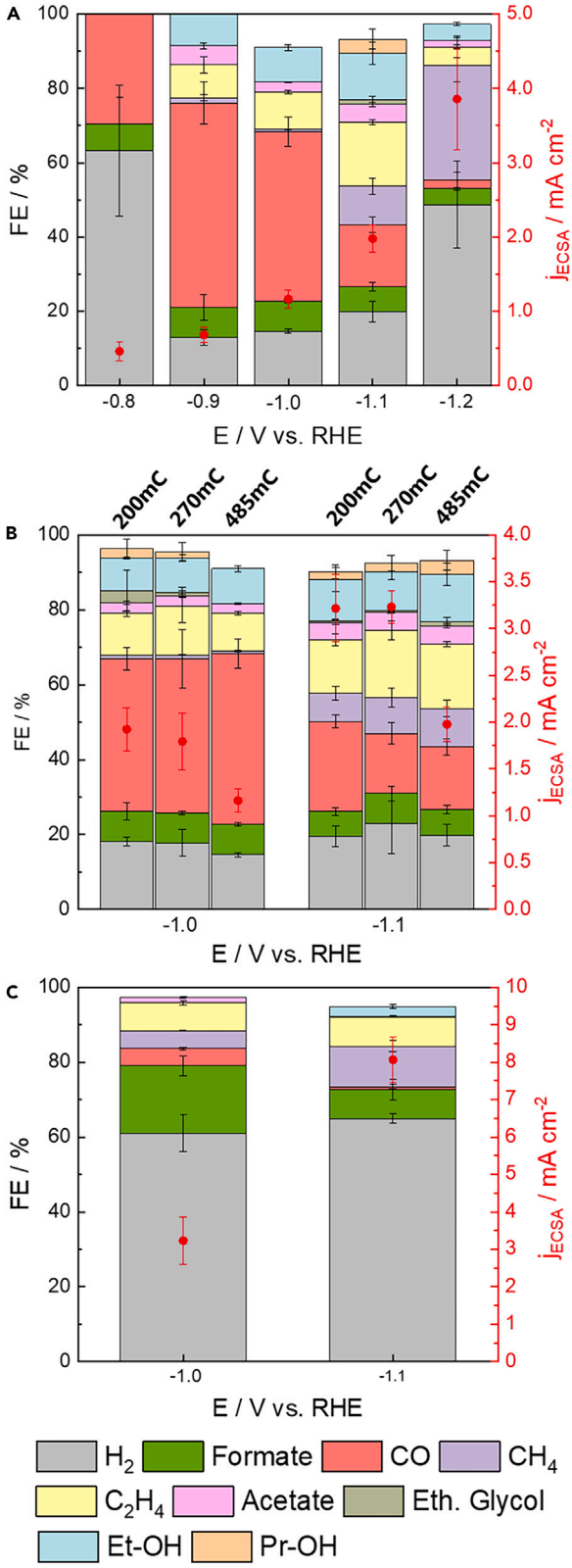
A
FE / %
jECSA / mA cm-2
E / V vs. RHE
-0.8
-0.9
-1.0
-1.1
-1.2
B
200mC
270mC
485mC
200mC
270mC
485mC
FE / %
jECSA / mA cm-2
E / V vs. RHE
-1.0
-1.1
C
FE / %
jECSA / mA cm-2
E / V vs. RHE
-1.0
-1.1
H2
Formate
CO
CH4
C2H4
Acetate
Eth. Glycol
Et-OH
Pr-OH

Figure 2. Product selectivity of 3Cu:1Ag under conditions of CO_2 reduction

(A and B) (A) Product distribution after 1 h of reaction, depending on the potential (from −0.8 to −1.2 V_{RHE}) at −485 mC and, (B) product distribution after 1 h reaction for the optimal potentials (−1.0 and −1.1 V_{RHE}) for the three coverages (−200, −270, and −485 mC).

(C) Product selectivity of Cu nanostructures at −485 mC and the optimal potentials after 1 h CO_2RR. Data are represented as mean ± FE (black error bar) and ± mA cm^{-2}.

composition of the deposits in bulk does not change while increasing the loading and there is only a change in the NPs size. We ascribe these results to the fact that the deposition rates of Cu and Ag are similar and both metals are well mixed in the bulk. However, the surface composition could change due to the lower surface energy of silver or because of air exposure or dissolution/redeposition of copper after bringing the nanostructures to open circuit potential.[66–68]

Before testing these nanostructures for CO_2RR, we have determined the ECSA and roughness factor (R) of each sample using voltammetric lead UPD, to assess their intrinsic activity or activity normalized by surface active sites during the CO_2RR. The R gives us the increase in the active area in relation to the geometric area.[69,70] Figure 1C shows the Pb UPD voltammograms of the 3Cu:1Ag nanostructures from Figure 1A (black line) and 1B (blue line). The lead UPD on the 3Cu:1Ag nanostructures shows a pair of quasi-reversible peaks, a single broad and intense peak centered at 0.12 V_{RHE} in the cathodic scan, with its counterpart at 0.15 V_{RHE} in the anodic scan. The lack of sharp peaks indicates that we have deposited polycrystalline structures with any preferential orientation.[57] The Pb UPD current intensity increases with the loading as well as with the size of the nanostructures, indicating that the larger nanostructure deposited at −485 mC has a higher roughness factor than the sample at −200 mC. The calculated ECSA and R are 4.86 cm^2 and 0.92 for the black line and 8.18 cm^2 and 1.54 for the blue line, respectively. The fact that the R is close to one in both cases is likely because we are only depositing a few dispersed nanostructures on the glassy carbon without covering the substrate. In Table S1 of the S.I, we have summarized the estimated ECSA and R of each Cu-Ag deposit of this study.

After preparing the 3Cu:1Ag nanostructures, we tested their performance toward CO_2RR in a 0.1 M $KHCO_3$ solution, using an H-cell setup connected to the online glassy carbon (GC) to investigate the product selectivity, as described in the Methods section. First, we investigated the product distribution at different reaction potentials from −0.8 V_{RHE} to −1.2 V_{RHE}. Figure 2A shows the faradaic efficiencies and current densities normalized by the ECSA of the 3Cu:1Ag deposit at −485 mC. The data from the deposits at −200 mC and −270 mC are illustrated in Figure S8 of the S.I. At the lowest overpotential of −0.8 V_{RHE}, we only obtain H_2, CO, and formate, whereas no liquid multi-carbon products are detected. At −0.9 V_{RHE}, the H_2 already drops to 13%, the CO production increases to 55%, and we start detecting C_{2+} products, i.e., C_2H_4 and acetate. The intermediate overpotentials of −1.0 V and −1.1 V_{RHE} are the optimal potentials to produce liquid C_{2+} products since H_2 stays under 23%, the production of CO is reduced, and C_2H_4 increases together with the production of liquid C_{2+} products. When adding Ag to the Cu, the competing HER is suppressed between −0.9 and −1.1 V_{RHE}. Our results align with other works reported in the literature on Cu-Ag catalysts, which also show a decrease of the H_2, and an increase in the production of both CO and liquid oxygenates (acetaldehyde, ethanol, and propanol) compared to single copper NPs.[21,37,39,71] For higher overpotentials, H_2 drastically doubles its value, and CH_4 production becomes dominant as it occurs on pure copper.[37,72]

We have addressed the catalytic performance of our deposited nanostructures at the applied potentials of −1.0 and −1.1 V_{RHE} and under 1 h of CO_2RR, to assess the selectivity changes of ethylene versus liquid C_{2+} products. Figure 2B represents the faradaic efficiencies and normalized current densities of the 3Cu:1Ag at the three prepared loadings of −200, −270, and −485 mC. We present the average of three different measurements of each sample with their corresponding standard deviations from triplicate measurements. The total faradaic efficiencies of our nanostructures are in good agreement with the values reported in the literature for other Cu and Cu-Ag systems at similar applied potentials.[26,30,37] For a more in-depth analysis, we have summarized in the S.I. the average faradaic efficiencies (%) and the intrinsic partial currents normalized by the ECSA (mA cm^{-2}) in Table S2, Table S3, and Table S4 for −200, −270, and −485 mC, respectively. The three samples exhibit a similar product selectivity which we attribute to the fact that the surface and bulk composition are similar. Only the sample at −485 mC shows a slight decrease in intrinsic activity which could be related with the differences in size and structure. At both optimal potentials, the H_2 remains suppressed below 23% while the CO goes up to 46% at −1.0 V_{RHE} and decreases to between 16% and 24% at −1.1 V_{RHE}. Ethanol is the most produced liquid C_{2+} product. Both ethylene and ethanol are more favored at −1.1 V_{RHE} with an average of 16% C_2H_4 and 12% C_2H_6O in contrast to 11% and 9% at −1.0 V_{RHE}. The other liquid C_{2+} products, i.e., propanol, acetate, and ethylene glycol vary in low proportions between both potentials. The production of liquid C_{2+} products reaches 20% at −1.1 V_{RHE} while it remains at 17% at −1.0 V_{RHE}. However, if we evaluate the relationship between C_{2+} products and ethylene, the liquid C_{2+}/C_2H_4 ratio is 1.5 at −1.0 V_{RHE} while it is 1.2 at −1.1 V_{RHE}. Our production distribution results and the intrinsic currents after 1 h of CO_2RR at the 3Cu:1Ag nanostructures are close to the values of several Cu-Ag systems from the literature.[36,37] We observed that the H_2 and CO production drops down whereas the C_{2+} products become higher, with C_2H_4 stopping being the dominant product and liquid C_{2+} products equaling their faradaic efficiency.

To assess the effect of silver in the production rate of C_{2+} products as well as on the selectivity toward liquid oxygenates, we electrodeposited pure Cu nanostructures from DES at −1.05 $V_{Ag|AgCl}$ with the same loadings and carried out CO_2RR. Figures S4A and S4B show the Cu nanostructures at −200 and −485 mC, respectively. The NPs present a flower shape with a diameter close to 300 nm. The size remained the same while the coverage of the deposit clearly increased from −200 to −485 mC. This morphology is in good agreement with previous works on Cu electrodeposition from DES in GC.[59] Similarly to the 3Cu:1Ag, the Pb UPD current intensity also increases with the loading of the nanostructures. Figures S10A and S11 show the Pb UPD of the Cu nanostructures. The calculated R and mass loadings are 0.47 and 0.07 g for −200 mC, 0.64 and 0.09 g for −270 mC, and 1.04 and 0.16 g for −485 mC.

Figure 2C illustrates the CO_2RR efficiencies and total intrinsic current densities at the optimal potentials of −1.0 and −1.1 V_{RHE} of our Cu nanostructures at −485 mC. The values and partial intrinsic currents of each product for the sample at −485 mC are also summarized in

Table S5. At both chosen overpotentials, we have observed a huge increase in the H_2 production compared to 3Cu:1Ag nanostructures. A 58% and 66% of H_2 were detected at −1.0 and −1.1 V_{RHE}, respectively. On the contrary, CO production has decreased to a 4% at −1.0 V_{RHE} while it was mainly negligible at −1.1 V_{RHE}. The faradaic efficiency of ethylene stayed near 8% at both potentials, far from the 16% and 22% from 3Cu:1Ag at −1.1 V_{RHE}. At −1.0 V_{RHE}, we have detected 1% of acetate and no ethanol, propanol, or ethylene glycol. The main product after H_2 was formate. At −1.1 V_{RHE}, 3% of ethanol was detected, but propanol or ethylene glycol had not been detected. These efficiency values are far from the efficiency value of 20% for C_{2+} liquids obtained on the 3Cu:1Ag at −1.1 V_{RHE}. We have noticed that while copper nanostructures prepared at −270 and −485 mC have exhibited similar results, the sample at −200 mC has produced no ethanol at −1.1 V_{RHE} and more CO and formate production. We attribute this change in selectivity to a possible dissolution when the coverage is too low. This can be expected from the poor coverage and different NP sizes observed from the SEM image at −200 mC before reaction, and the changes in size and morphology of this sample after reaction (Figure S4). Studies on small copper NPs have reported the possible dissolution or redeposition of the copper once the catalyst is in contact with the alkaline electrolyte when there is no potential control or when first applying a reduction potential.[67,68,73]

Our Cu nanostructures have not exhibited a high efficiency toward liquid C_{2+} products; instead, they are more selective toward H_2 production. Some studies in the literature have reported that poly-oriented copper NPs with small size and high number of defect and corner sites promote the formation of H_2. We hypothesize that the high activity toward hydrogen in our nanostructures might be related with a lack of ordering, the absence of C_{2+}-selective sites, and a high number of edges and defects.[74,75] Even though ethylene is the major C_{2+} product obtained on our Cu nanostructures at −485 mC, its faradaic efficiency is lower (7.9%) than in Cu-Ag nanostructures (18% at −485 mC). In contrast, the partial intrinsic current for ethylene in Cu is higher than that on 3Cu:1Ag, whereas the partial currents of the generated C_{2+} products are similar in both Cu and Cu-Ag electrocatalysts. We observe that by increasing the presence of silver in the bimetallic nanostructure, the intrinsic current of CO increases and that of C_{2+} slightly decreases compared to pure copper. We have ascribed this result to the silver-rich samples containing more electrode areas covered by silver, which produces CO, and fewer copper sites to produce C_{2+} products. Lead UPD is a surface-sensitive technique that allows estimating the number of sites on the surface, considering that the lead coverage is similar on both silver and copper, and the difference in charge is minimal and related to the difference in atomic ratio. Despite that, lead UPD does not unfortunately provide information on which sites are silver and which ones are copper. The lead UPD profiles provide a single broad peak that differs from either pure copper or pure silver, possibly because the electronic structure of the bimetallic Cu-Ag is different from that of the separated metal phases. These results suggest that the suppression of the H_2 on Cu-Ag compared to Cu is one key aspect that improves the product selectivity when adding silver to copper. Previously, Bell and co-workers showed that Cu-Ag polished alloys and Cu(100) surfaces modified with silver presented an enhancement of selectivity because silver primarily suppressed the formation of hydrogen.[39] Bell and co-workers suggested that the addition of silver increases the surface oxophobicity and induces a compressive strain effect on copper that results in the reduction of the binding energies of H and O relative to CO. This change in the electronic structure enhances the selectivity for the production of C_{2+} products derived from CO because of the selective suppression of HER, i.e., the HER current dropped down but the C_{2+} essentially did not change. Using angle-resolved XPS the authors observed that silver was shifting the valence state of copper to higher binding energies. Other proposals to explain the enhanced selectivity by silver suggest that silver increases the local concentration of CO, increasing the CO coverage on copper or facilitating the C-C coupling reaction.[30,37] Finding an explanation for the higher production of oxygenates over ethylene is more complex. Previous reports suggest that both ethylene and oxygenates come from the same dimer intermediate which deviates to the ethanol or alcohol pathway when silver is added to copper. One possible reason for this change in the mechanism pathway could be that silver reduces the hydrogen formation and coverage avoiding further hydrogenation of the OC-CO dimer.[9,22,39,76]

Figure 3 shows the SEM images and EDS maps of the 3Cu:1Ag nanostructures at −200 and −485 mC after 1 h of CO_2RR. Neither the morphology nor the composition changed after reaction according to the low-resolution images. Interestingly, despite the high surface diffusion on glassy carbon, we do not observe coalescence or agglomeration of the nanostructures after 1 h of reaction. Figures S4B and S4D exhibit the SEM images of the pure electrodeposited Cu samples at −200 and −485 mC after 1 h of reaction at −1.1 V_{RHE}. The size and distribution of the NPs did not considerably change after reaction. However, even though the Cu NPs did not agglomerate under reaction conditions, we noticed a slightly more rounded shape in the sample at −200 mC which confirms our hypothesis of dissolution and poor stability when the coverage is too low, in agreement with other works.[67,77–79]

To evaluate the changes in the CO_2RR efficiency with the Cu/Ag ratio, we have prepared nanostructures richer in Cu using a 6Cu:1Ag molar ratio bath solution and by applying a potential of −0.68 V_{RHE}. Like the 3Cu:1Ag nanostructures, we have prepared three loadings of −200, −270, and −485 mC with the 6Cu:1Ag bath composition. Figure 4A shows the SEM image and EDS maps at −485 mC before reaction. The morphology of the NPs has the same rounded shape with porosity as the 3Cu:1Ag. The size is slightly smaller, and the diameter is around 300 nm. The XPS spectra of this sample can also be found in Figure S7C and S7D of the S.I, with a surface composition of 1.7:1 of Cu and Ag after 20 s of sputtering. The calculated mass loadings based on the EDS results are 0.1 mg for −200 mC, 0.13 mg for −270 mC, and 0.23 mg for −485 mC. Figure 4B shows the SEM and EDS maps after 1 h of CO_2RR at −1.1 V_{RHE} where the morphology did not change. The EDS analysis shows that the bulk composition varied between 4:1 and 2.5:1 Cu to Ag ratio before (obtained by quantification from EDS color maps from Figure 4A) and after 1 h of CO_2RR (color maps from Figure 4B). The SEM images of the 6Cu:1Ag deposits at −200 and −270 mC can be found in Figures S5A and S5B of the S.I. At lower loadings, the NPs presented the same morphology but a smaller diameter of 200 nm. We have also estimated the ECSA and R of the 6Cu:1Ag nanostructures by Pb UPD, as shown in Figure S10B. The ECSA and R from the sample of Figure 4A are 7.48 cm^2 and 1.42, respectively.

Figure 4C exhibits the CO_2RR efficiencies and total intrinsic current density at −1.1 V_{RHE} of the 6Cu:1Ag nanostructures at the three loadings. Tables S6, S7 and S8 in the S.I. show the faradaic efficiency values and partial intrinsic current densities of each product for the −200,

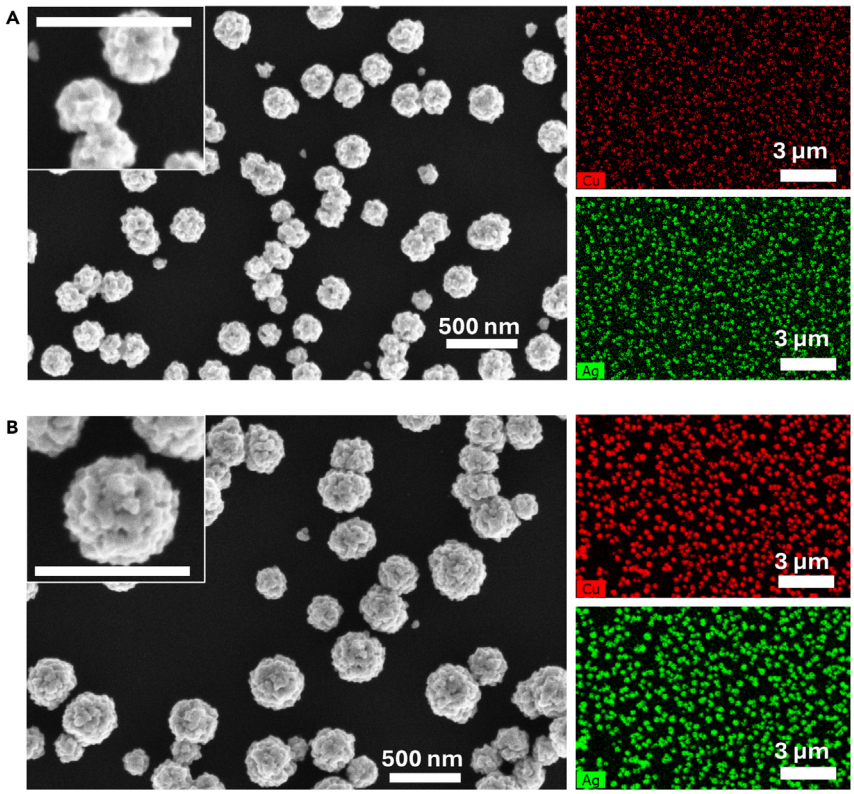

Figure 3. SEM and EDS characterization after 1 h of reaction of 3Cu:1Ag samples deposited at different circulated charges
(A and B) (A) Sample deposited at −200 mC and (B) sample deposited at −485 mC. The scale bars on the inlet SEM images correspond to 500 nm.

−270, and −485 mC, respectively. We noticed a slight decrease in the total faradaic efficiency on the sample of −200 mC at −1.1 V_{RHE}, which we attribute to the higher copper content that might induce some dissolution/reprecipitation as explained for the least covered copper sample. The results at −1.0 V_{RHE} are illustrated in Figure S9. We did not add the results at −1.0 V_{RHE} here since no ethanol, propanol, or ethylene glycol was detected at this potential when the amount of Cu slightly increases on the nanostructure. At −1.1 V_{RHE}, propanol and acetate are detected although ethylene glycol was not detected. This result remarks the importance of controlling the Cu/Ag ratio in the nanostructures to increase the production of liquid C_{2+} products over ethylene. Additionally, H_2 remains suppressed between 17% and 21%, similar to the results on 3Cu:1Ag nanostructures. We have also observed that the product selectivity toward CO and CH_4 changes with the circulated charge or the mass loading of the deposited nanostructures. CO decreases with the increase in mass loading from 19% (−200 mC) to 9% (−485 mC) while CH_4 increases from 9% to 16%, approaching more to the behavior of pure copper. We ascribe this fact to that copper electrodeposition is slightly faster than silver for this bath composition due to the higher copper concentration in solution, which may result in a slight increase of the amount of copper at the surface at longer times of electrodeposition or for higher loadings. Ethylene slightly increases as well with the coverage from 15% to 22%. The liquid C_{2+} products represent 19%–17% from −200 to −485 mC. Ethanol remained the major liquid C_{2+} product with an average of 10%. If we compare these results with the selectivity trends found for the 3Cu:1Ag nanostructures, H_2 remained suppressed, CO became slightly lower, and C_2H_4 and Et-OH were still the major C_{2+} products. We attributed the lower CO and higher C_2H_4 values to the lower silver content. The 6Cu:1Ag deposits behave more similar to pure copper in which it was proven that less CO is available, and ethylene is the most favored C_{2+} product.[19,26,30,37]

DISCUSSION

In this section, we aim to gain a deeper understanding on the structure-activity-selectivity relations and assess the effect of silver on our nanostructures. Figure 5 shows an overview of the partial intrinsic current densities, *i.e.*, the current densities in relation to the number of active surface sites (normalized by the ECSA), of 3Cu:1Ag, 6Cu:1Ag, and pure Cu at −485 mC after 1 h of CO_2RR at −1.1 V_{RHE}. Figure 5A shows C_2H_4 versus the rest of the liquid C_{2+} products. When adding silver, the ethylene partial current starts to decrease since the surface stops behaving like pure Cu, which promotes ethylene production. Cu-Ag facilitates the pathway toward the formation of liquid alcohols and oxygenates.[39] Concerning the production of liquid C_{2+} products, there is not a huge change in the intrinsic partial current densities within the different Cu/Ag ratios. Ethanol and acetate intrinsic partial current densities remain close in the 3 samples while propanol is promoted in the samples richer in silver.[17]

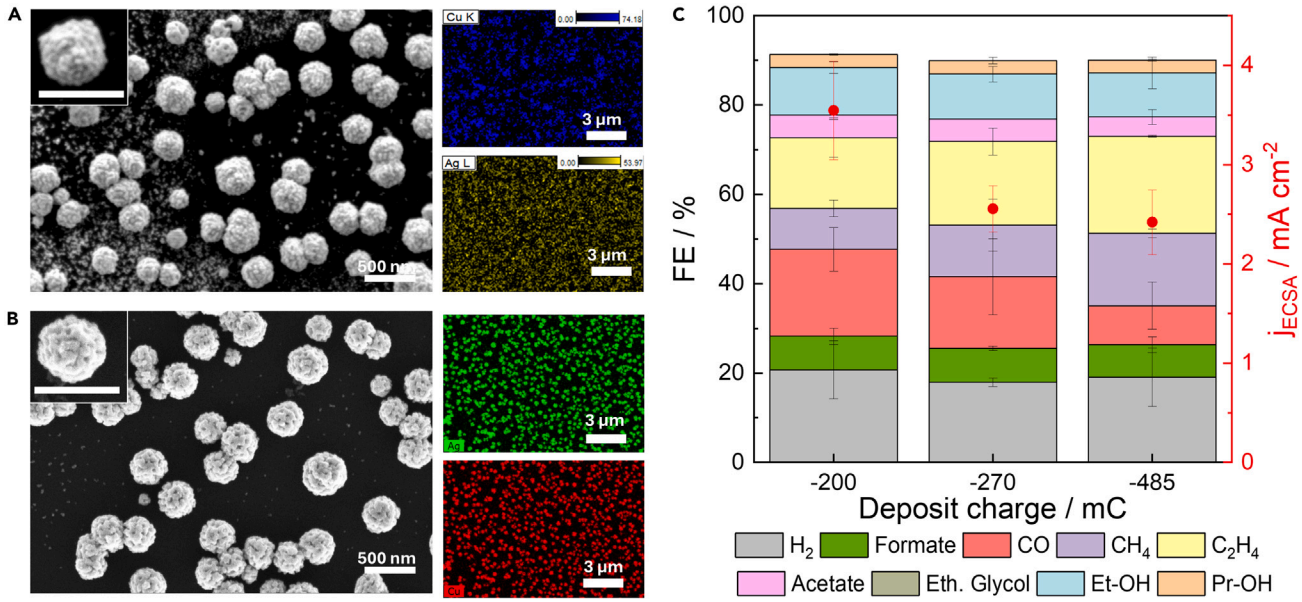

Figure 4. Analysis of the surface morphology with SEM and composition with EDS of electrodeposited 6Cu:1Ag

(A and B) (A) SEM and EDS before reaction (EDS at Topsoe) at −485 mC (B) SEM and EDS after 1 h of reaction (EDS at EPFL) at −485 mC. The scale bars on the inlet images correspond to 500 nm.

(C) Product distribution at −1.1 V_{RHE} for −200, −270, and −485 mC. Data are represented as mean +/− FE (black error bar) and +/− mA cm^{-2}.

Figure 5B illustrates the intrinsic partial current densities of all the CO_2RR products and H_2 on the three different Cu and Cu-Ag nanostructures. From Cu nanostructures to 6Cu:1Ag and 3Cu:1Ag, we have noticed a clear suppression of the H_2, an increase of CO, and a decrease of CH_4 and formate. However, the partial current densities of the total production of C_{2+} molecules remain similar in the three deposits. Our results show that the addition of Ag primarily reduces the formation of hydrogen but does not cause a substantial increase of the C_{2+} products. A plausible explanation for the suppression of H_2 might be that Ag is sited on the Cu undercoordinated sites, which are attributed to promoting H_2, blocking its production.[30,74] An alternative explanation might be a weakening of the *H adsorption energy by a compressive strain effect induced in Cu when Cu and Ag are mixed. We have discussed how previous reports on extended Cu-Ag alloy surfaces and Cu(100) modified with silver showed that the product selectivity enhancement was primarily due to a suppression of hydrogen, whereas the production of C_{2+} did not substantially change.[39] We have observed essentially the same behavior on our Cu-Ag nanostructures. However, to reach the same conclusion, it was necessary to electrochemically determine the ECSA and address the intrinsic partial currents. Our study highlights the importance of developing methods that allow to quantitatively address the active area and structure of nanostructured catalysts and NPs to provide a rational explanation of the catalytic performance enhancement. We attribute the reduction of CH_4 production to the lower availability of adsorbed *H, necessary for the hydrogenation of this molecule as it has been already discussed by Hori and co-workers.[72]

The similar intrinsic partial current densities of C_{2+} products for all the samples might indicate that the limiting step that controls the reaction rate to produce C_{2+} products is not affected by the pH or hydrogen production. Instead, it might be related to the formation of a carbon-carbon dimer through the C-C coupling step, as discussed by Koper and co-workers in previous reports.[4,80,81] The dimer is the precursor and common intermediate in the production of ethylene, acetaldehyde, ethanol, and also propanol after the insertion of a CO molecule.[9,13,21,82] Although Ag does not change the partial rates of C_{2+} products formation, likely because it does not substantially affect the carbon-carbon dimerization step energetics, it promotes the pathway toward the formation of alcohols and oxygenates over ethylene. The groups of Calle-Vallejo and Yeo already observed an increase of ethanol over ethylene when adding Ag to oxide-derived Cu nanowires.[37] Sargent and co-workers have also shown a Cu/Ag electrode which destabilizes the ethylene reaction pathway promoting ethanol instead.[9] Interestingly, we can smoothly tailor the product distribution toward ethylene and liquid alcohols by tuning the Cu/Ag ratio in our nanostructures deposited in a DES. This change in product selectivity could be related with a change in the electronic structure of copper, due to strain or ligand effects induced by silver, which increase the CO coverage and reduce the adsorption of *H thus promoting the formation of oxygenates and alcohols.[36,39] However, it is important to remark that our Cu-Ag nanostructures do not intrinsically enhance the production of C_{2+} products over Cu. Indeed, we notice that the partial current densities of C_{2+} in 3Cu:1Ag slightly decay in comparison to Cu-rich nanostructures, fact that we ascribe to an increased amount of surface Ag sites that do not contribute to reduce CO_2 to hydrocarbons but to produce more CO. We note that the production of CO considerably increases from Cu to 3Cu:1Ag whereas the formate decays, as observed in the inset of Figure 5B, which suggests an increase of silver sites over copper sites on the surface and during the reaction. Since the shape and size of the Cu-Ag bimetallic nanostructures have barely changed before and after reaction, we believe there is no significant dissolution

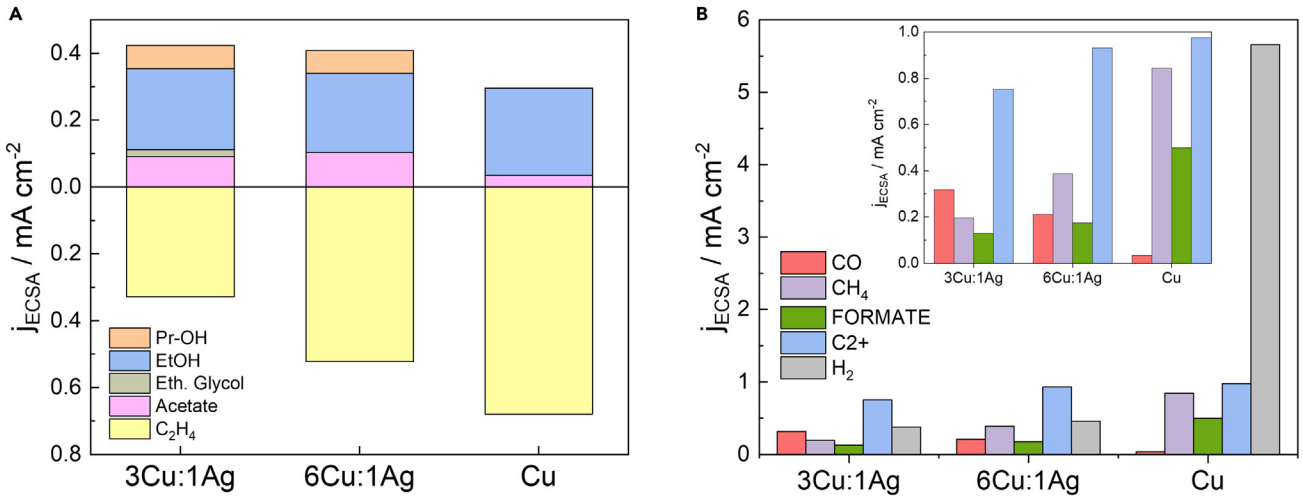

Figure 5. C_{2+} compared with the rest of the products after 1 h of CO_2 reduction at -1.1 V_{RHE}

(A) Liquid C_{2+} products versus ethylene represented against the partial currents normalized by the ECSA for 3Cu:1Ag, 6Cu:1Ag, and Cu at −485 mC. (B) Total C_{2+} products of the same samples compared with the rest of the products.

or redeposition of the copper when the electrodes are in contact with the electrolyte. However, we have considered this possibility for the pure copper nanostructures as stated previously.[73] To address how surface composition and structure might change at each applied potential condition and/or under different reaction times, we will need to carry out *in situ* operando surface and spectroscopy characterization techniques.

Our work elucidates the importance of estimating the ECSA to analyze the intrinsic activity of our nanocatalysts under reaction conditions and assess the main effects on selectivity. It is important to remark that the product selectivity and intrinsic activity of our electrodeposited catalysts have been measured in a classical electrochemical H-cell where the amount of dissolved CO_2 that is converted at the electrode surface is low. Our results are in line with other Cu-Ag systems under the same conditions, as discussed earlier.[36,37,39] However, recent results on CO_2RR in gas diffusion electrodes (GDEs) have shown that Ag-doped Cu catalysts display a high 80% selectivity toward the formation of C_{2+} with propanol being the major C_{2+} liquid product.[17] Another recent study on CO_2RR in GDEs has presented Ag-modified Cu oxide-derived catalysts exhibiting up to 90% selectivity for the production of C_{2+} products with ethanol being the major liquid C_{2+} product.[83] GDE reduces the CO_2 mass transport limitation, allows tuning of the CO_2 partial pressure, controls better the concentration of CO_2 that reaches the surface and parameters that affect the CO surface coverage, and can ultimately enhance the C-C coupling step to form C_{2+}.[84–86] To verify if the production of C_{2+} products on our Cu-Ag nanostructures improves with the addition of silver, future work using GDEs to investigate the intrinsic partial current densities normalized by the ECSA needs to be analyzed. These studies will be key to elucidate the structure-activity-selectivity relations under realistic conditions of our nanostructures.

Conclusions

Herein, we have prepared active Cu-Ag nanostructures with tunable product selectivity for the CO_2RR. We have investigated the performance of our bimetallic nanostructures toward the CO_2RR and addressed how the addition of silver affects the intrinsic partial current density of each product. We highlight the importance of determining the ECSA to report the intrinsic partial activities and decouple the effects of mixing Ag with Cu with those of having different structures in both the selectivity and activity. Our results show that the main improvement in selectivity toward C_{2+} products is due to a suppression of the hydrogen formation on Cu after adding Ag. Although we observe that Ag promotes the formation of alcohols and oxygenates, it does not cause a substantial change in the rate of formation of C_{2+} products. To improve the partial current densities of liquid C_{2+}, it would be necessary to prepare Cu-Ag particles with tuned surface structure and large active surface areas.

Limitations of this study

We evaluated the intrinsic performance of electrodeposited Cu-Ag nanostructures toward the reduction CO_2. By calculating the electroactive surface area of the deposited nanostructures, we observed that silver intrinsically suppresses the HER and favors the formation of liquid oxygenates. The determination of the electroactive surface area by lead UPDs only gives an approximate value of the total number of surface sites. However, our methods do not give information on how silver and copper are distributed on the surface. It is, therefore, uncertain which specific structure site is responsible for the production of liquids on our Cu-Ag catalysts. We hypothesized that silver changes the electronic structure and decreases the oxophilicity of the bimetallic surface, causing the suppression of hydrogen. Further, *in situ* and/or operando spectroscopic and microscopic methods are crucial to elucidate the nature of the atomic active sites and molecular intermediates and precisely assess how the copper-silver bond modifies the product selectivity of copper.

STAR★METHODS

Detailed methods are provided in the online version of this paper and include the following:

- KEY RESOURCES TABLE
- RESOURCE AVAILABILITY
  - Lead contact
  - Materials availability
  - Data and code availability
- EXPERIMENTAL MODEL AND STUDY PARTICIPANTS DETAILS
- METHOD DETAILS
  - Preparation of the nanostructured Cu-Ag deposits from DES
  - CO_2 electroreduction (CO_2RR) measurements and analysis
  - Determination of faradic efficiencies and partial currents of the CO_2RR products on different Cu and Cu-Ag nanostructures
  - Pb underpotential deposition (UPD) and estimation of the ECSA and roughness factor (R)
  - Determination of the mass loading of Cu and Cu-Ag
  - Morphological and compositional analysis
- QUANTIFICATION AND STATISTICAL ANALYSIS
- ADDITIONAL RESOURCES

SUPPLEMENTAL INFORMATION

Supplemental information can be found online at https://doi.org/10.1016/j.isci.2024.109933.

ACKNOWLEDGMENTS

We acknowledge support from the Danish National Research Foundation Center for High Entropy Alloy Catalysis (CHEAC, DNRF149). We also acknowledge the Villum Foundation for financially supporting this project through a Villum Young Investigator Grant (project number: 19142). This work was also supported by the Danish Foundation through the DFF-Research Project1 (Thematic Research, green transition) grant with number: 0217-00213A. P.S.P. gratefully acknowledges the Villum Foundation for its financial support (project number: 53090). V.O. acknowledges the support from the Swiss National Science Foundation (SNSF) under grant number 200021L_191997/1. This project has also received funding from Villum Fonden V-SUSTAIN (grant number: 9455). We finally acknowledge Prof. Raffaella Buonsanti from EPFL for providing the facilities to perform most of the experiments of this study as well as valuable discussions.

AUTHOR CONTRIBUTIONS

E.P.-M.: investigation, methodology, formal analysis, data curation, writing – original draft, and visualization. V.O.: *ex situ* characterization, investigation, formal analysis, data curation, and writing – review and editing. K.N.D.: *ex situ* characterization, investigation, formal analysis, data curation, and writing – review and editing. H.F.: resources and writing – review and editing. I.C.: data curation, resources, and writing – review and editing. P.S.-P: supervision, methodology, conceptualization, writing – original draft, visualization, and project administration. M.E.-E.: supervision, methodology, conceptualization, writing – review and editing, project administration, and funding acquisition.

DECLARATION OF INTERESTS

The authors declare no competing interests.

Received: January 25, 2024
Revised: March 14, 2024
Accepted: May 5, 2024
Published: May 7, 2024

REFERENCES

1. Calvin, K., Dasgupta, D., Krinner, G., Mukherji, A., Thorne, P.W., Trisos, C., Romero, J., Aldunce, P., Barrett, K., Blanco, G., et al. (2023). IPCC, 2023: Climate Change 2023: Synthesis Report. Contribution of Working Groups I, II and III to the Sixth Assessment Report of the Intergovernmental Panel on Climate Change [Core Writing Team, H. Lee and J. Romero. In IPCC, P. Arias, M. Bustamante, I. Elgizouli, G. Flato, M. Howden, C. Méndez-Vallejo, J.J. Pereira, R. Pichs-Madruga, S.K. Rose, and Y. Saheb, et al., eds. (Geneva, Switzerland). https://doi.org/10.59327/IPCC/AR6-9789291691647.
2. Sebastián-Pascual, P., Mezzavilla, S., Stephens, I.E.L., and Escudero-Escribano, M. (2019). Review: Structure-Sensitivity and Electrolyte Effects in CO2 Electroreduction: From Model Studies to Applications. ChemCatChem. https://doi.org/10.1002/cctc.201900552.
3. Sheehan, S.W., and Buonsanti, R. (2021). Deriving Value from CO2: From Catalyst Design to Industrial Implementation (Preprint at Elsevier Inc.). https://doi.org/10.1016/j.checat.2021.08.010.
4. Birdja, Y.Y., Pérez-Gallent, E., Figueiredo, M.C., Göttle, A.J., Calle-Vallejo, F., and Koper, M.T.M. (2019). Advances and challenges in understanding the electrocatalytic conversion of carbon dioxide to fuels. Nat. Energy *4*, 732–745.

https://doi.org/10.1038/s41560-019-0450-y.

5. Stephens, I.E.L., Chan, K., Bagger, A., Boettcher, S.W., Bonin, J., Boutin, E., Buckley, A.K., Buonsanti, R., Cave, E.R., Chang, X., et al. (2022). 2022 roadmap on low temperature electrochemical CO2 reduction. JPhys Energy *4*, 042003. https://doi.org/10.1088/2515-7655/ac7823.
6. Xu, D., Li, K., Jia, B., Sun, W., Zhang, W., Liu, X., and Ma, T. (2023). Electrocatalytic CO2 reduction towards industrial applications (Preprint at John Wiley and Sons Inc). https://doi.org/10.1002/cey2.230.
7. Nitopi, S., Bertheussen, E., Scott, S.B., Liu, X., Engstfeld, A.K., Horch, S., Seger, B., Stephens, I.E.L., Chan, K., Hahn, C., et al. (2019). Progress and Perspectives of Electrochemical CO2 Reduction on Copper in Aqueous Electrolyte. Chem. Rev. *119*, 7610–7672. https://doi.org/10.1021/acs.chemrev.8b00705.
8. Wang, P., Yang, H., Tang, C., Wu, Y., Zheng, Y., Cheng, T., Davey, K., Huang, X., and Qiao, S.Z. (2022). Boosting electrocatalytic CO2–to–ethanol production via asymmetric C–C coupling. Nat. Commun. *13*, 3754. https://doi.org/10.1038/s41467-022-31427-9.
9. Li, Y.C., Wang, Z., Yuan, T., Nam, D.H., Luo, M., Wicks, J., Chen, B., Li, J., Li, F., De Arquer, F.P.G., et al. (2019). Binding Site Diversity Promotes CO2 Electroreduction to Ethanol. J. Am. Chem. Soc. *141*, 8584–8591. https://doi.org/10.1021/jacs.9b02945.
10. Schouten, K.J.P., Calle-Vallejo, F., and Koper, M.T.M. (2014). A step closer to the electrochemical production of liquid fuels. Angew. Chem. Int. Ed. Engl. *53*, 10858–10860. https://doi.org/10.1002/anie.201406174.
11. Wang, X., Ou, P., Ozden, A., Hung, S.F., Tam, J., Gabardo, C.M., Howe, J.Y., Sisler, J., Bertens, K., García de Arquer, F.P., et al. (2022). Efficient electrosynthesis of n-propanol from carbon monoxide using a Ag–Ru–Cu catalyst. Nat. Energy *7*, 170–176. https://doi.org/10.1038/s41560-021-00967-7.
12. Wang, X., Wang, Z., García de Arquer, F.P., Dinh, C.T., Ozden, A., Li, Y.C., Nam, D.H., Li, J., Liu, Y.S., Wicks, J., et al. (2020). Efficient electrically powered CO2-to-ethanol via suppression of deoxygenation. Nat. Energy *5*, 478–486. https://doi.org/10.1038/s41560-020-0607-8.
13. Gao, D., Arán-Ais, R.M., Jeon, H.S., and Roldan Cuenya, B. (2019). Rational Catalyst and Electrolyte Design for CO2 Electroreduction towards Multicarbon Products. Preprint at (Nature Publishing Group). https://doi.org/10.1038/s41929-019-0235-5.
14. Ledezma-Yanez, I., Gallent, E.P., Koper, M.T., and Calle-Vallejo, F. (2016). Structure-sensitive electroreduction of acetaldehyde to ethanol on copper and its mechanistic implications for CO and CO2 reduction. Catal. Today *262*, 90–94. https://doi.org/10.1016/j.cattod.2015.09.029.
15. Bian, B., Shi, L., Katuri, K.P., Xu, J., Wang, P., and Saikaly, P.E. (2020). Efficient solar-to-acetate conversion from CO2 through microbial electrosynthesis coupled with stable photoanode. Appl. Energy *278*, 115684. https://doi.org/10.1016/j.apenergy.2020.115684.
16. Yang, Q., Liu, X., Zhu, S., Huang, W., and Zhang, D. (2019). Efficient Utilization of CO 2 in a Coal to Ethylene Glycol Process Integrated with Dry/Steam-Mixed Reforming: Conceptual Design and Technoeconomic Analysis. ACS Sustain. Chem. Eng. *7*, 3496–3510. https://doi.org/10.1021/acssuschemeng.8b05757.
17. Wang, X., Wang, Z., Zhuang, T.T., Dinh, C.T., Li, J., Nam, D.H., Li, F., Huang, C.W., Tan, C.S., Chen, Z., et al. (2019). Efficient upgrading of CO to C3 fuel using asymmetric C-C coupling active sites. Nat. Commun. *10*, 5186. https://doi.org/10.1038/s41467-019-13190-6.
18. Ripatti, D.S., Veltman, T.R., and Kanan, M.W. (2019). Carbon Monoxide Gas Diffusion Electrolysis that Produces Concentrated C2 Products with High Single-Pass Conversion. Joule *3*, 240–256. https://doi.org/10.1016/j.joule.2018.10.007.
19. Wang, M., Nikolaou, V., Loiudice, A., Sharp, I.D., Llobet, A., and Buonsanti, R. (2022). Tandem electrocatalytic CO2 reduction with Fe-porphyrins and Cu nanocubes enhances ethylene production. Chem. Sci. *13*, 12673–12680. https://doi.org/10.1039/d2sc04794b.
20. Christensen, O., Zhao, S., Sun, Z., Bagger, A., Lauritsen, J.V., Pedersen, S.U., Daasbjerg, K., and Rossmeisl, J. (2022). Can the CO2Reduction Reaction Be Improved on Cu: Selectivity and Intrinsic Activity of Functionalized Cu Surfaces (Preprint at American Chemical Society). https://doi.org/10.1021/acscatal.2c04200.
21. Kuhl, K.P., Cave, E.R., Abram, D.N., and Jaramillo, T.F. (2012). New insights into the electrochemical reduction of carbon dioxide on metallic copper surfaces. Energy Environ. Sci. *5*, 7050–7059. https://doi.org/10.1039/c2ee21234j.
22. Jaster, T., Gawel, A., Siegmund, D., Holzmann, J., Lohmann, H., Klemm, E., and Apfel, U.-P. (2022). iScience Electrochemical CO 2 Reduction toward Multicarbon Alcohols-The Microscopic World of Catalysts & Process Conditions. iScience. https://doi.org/10.1016/j.isci.2022.104010.
23. Hori, Y., Murata, A., Takahashi, R., and Suzuki, S. (1987). Electroreduction of carbon monoxide to methane and ethylene at a copper electrode in aqueous solutions at ambient temperature and pressure. J. Am. Chem. Soc. *109*, 5022–5023.
24. Mangione, G., Huang, J., Buonsanti, R., and Corminboeuf, C. (2019). Dual-facet mechanism in copper nanocubes for electrochemical CO2 Reduction into Ethylene. J. Phys. Chem. Lett. *10*, 4259–4265. https://doi.org/10.1021/acs.jpclett.9b01471.
25. Zhao, X., Du, L., You, B., and Sun, Y. (2020). Integrated Design for Electrocatalytic Carbon Dioxide Reduction (Preprint at Royal Society of Chemistry). https://doi.org/10.1039/d0cy00453g.
26. Rossi, K., and Buonsanti, R. (2022). Shaping Copper Nanocatalysts to Steer Selectivity in the Electrochemical CO2 Reduction Reaction. Acc. Chem. Res. *55*, 629–637. https://doi.org/10.1021/acs.accounts.1c00673.
27. Arán-Ais, R.M., Scholten, F., Kunze, S., Rizo, R., and Roldan Cuenya, B. (2020). The role of in situ generated morphological motifs and Cu(i) species in C2+ product selectivity during CO2 pulsed electroreduction. Nat. Energy *5*, 317–325. https://doi.org/10.1038/s41560-020-0594-9.
28. Hori, Y., Takahashi, I., Koga, O., and Hoshi, N. (2003). Electrochemical reduction of carbon dioxide at various series of copper single crystal electrodes. J. Mol. Catal. Chem. *199*, 39–47. https://doi.org/10.1016/S1381-1169(03)00016-5.
29. Morales-Guio, C.G., Cave, E.R., Nitopi, S.A., Feaster, J.T., Wang, L., Kuhl, K.P., Jackson, A., Johnson, N.C., Abram, D.N., Hatsukade, T., et al. (2018). Improved CO2 reduction activity towards C2+ alcohols on a tandem gold on copper electrocatalyst. Nat. Catal. *1*, 764–771. https://doi.org/10.1038/s41929-018-0139-9.
30. Iyengar, P., Kolb, M.J., Pankhurst, J.R., Calle-Vallejo, F., and Buonsanti, R. (2021). Elucidating the Facet-Dependent Selectivity for CO2Electroreduction to Ethanol of Cu-Ag Tandem Catalysts. ACS Catal. *11*, 4456–4463. https://doi.org/10.1021/acscatal.1c00420.
31. Ma, S., Sadakiyo, M., Heima, M., Luo, R., Haasch, R.T., Gold, J.I., Yamauchi, M., and Kenis, P.J.A. (2017). Electroreduction of carbon dioxide to hydrocarbons using bimetallic Cu-Pd catalysts with different mixing patterns. J. Am. Chem. Soc. *139*, 47–50. https://doi.org/10.1021/jacs.6b10740.
32. Dickinson, H.L., and Symes, M.D. (2022). Recent progress in CO2 reduction using bimetallic electrodes containing copper. Electrochem. Commun. *135*, 107212. https://doi.org/10.1016/j.elecom.2022.107212.
33. Vasileff, A., Xu, C., Jiao, Y., Zheng, Y., and Qiao, S.Z. (2018). Surface and Interface Engineering in Copper-Based Bimetallic Materials for Selective CO2 Electroreduction (Preprint at Elsevier Inc). https://doi.org/10.1016/j.chempr.2018.05.001.
34. Ren, D., Ang, B.S.H., and Yeo, B.S. (2016). Tuning the Selectivity of Carbon Dioxide Electroreduction toward Ethanol on Oxide-Derived CuxZn Catalysts. ACS Catal. *6*, 8239–8247. https://doi.org/10.1021/acscatal.6b02162.
35. Wang, Y., Wang, D., Dares, C.J., Marquard, S.L., Sheridan, M.V., and Meyer, T.J. (2018). CO2 reduction to acetate in mixtures of ultrasmall (Cu)n,(Ag)m bimetallic nanoparticles. Proc. Natl. Acad. Sci. USA *115*, 278–283. https://doi.org/10.1073/pnas.1713962115.
36. Qiao, Y., Kastlunger, G., Davis, R.C., Rodriguez, C.A.G., Vishart, A., Deng, W., Xu, Q., Li, S., Benedek, P., Chen, J., et al. (2023). Mechanistic Insights into Aldehyde Production from Electrochemical CO 2 Reduction on CuAg Alloy via Operando X-ray Measurements. ACS Catal. *13*, 9379–9391. https://doi.org/10.1021/acscatal.3c01009.
37. Ting, L.R.L., Piqué, O., Lim, S.Y., Tanhaei, M., Calle-Vallejo, F., and Yeo, B.S. (2020). Enhancing CO2 Electroreduction to Ethanol on Copper-Silver Composites by Opening an Alternative Catalytic Pathway. ACS Catal. *10*, 4059–4069. https://doi.org/10.1021/acscatal.9b05319.
38. Bagger, A., Ju, W., Varela, A.S., Strasser, P., and Rossmeisl, J. (2017). Electrochemical CO2 Reduction: A Classification Problem. ChemPhysChem *18*, 3266–3273. https://doi.org/10.1002/cphc.201700736.
39. Clark, E.L., Hahn, C., Jaramillo, T.F., and Bell, A.T. (2017). Electrochemical CO2 Reduction over Compressively Strained CuAg Surface Alloys with Enhanced Multi-Carbon Oxygenate Selectivity. J. Am. Chem. Soc. *139*, 15848–15857. https://doi.org/10.1021/jacs.7b08607.
40. Lee, S., Park, G., and Lee, J. (2017). Importance of Ag-Cu Biphasic Boundaries for Selective Electrochemical Reduction of CO2 to Ethanol. ACS Catal. *7*, 8594–8604. https://doi.org/10.1021/acscatal.7b02822.
41. You, H., Yang, S., Ding, B., and Yang, H. (2013). Synthesis of colloidal metal and metal

alloy nanoparticles for electrochemical energy applications. Chem. Soc. Rev. *42*, 2880–2904. https://doi.org/10.1039/C2CS35319A.

42. Tan, Y., Xue, X., Peng, Q., Zhao, H., Wang, T., and Li, Y. (2007). Controllable fabrication and electrical performance of single crystalline Cu2O nanowires with high aspect ratios. Nano Lett. *7*, 3723–3728. https://doi.org/10.1021/nl0721259.
43. Li, D., Wang, C., Tripkovic, D., Sun, S., Markovic, N.M., and Stamenkovic, V.R. (2012). Surfactant removal for colloidal nanoparticles from solution synthesis: The effect on catalytic performance. ACS Catal. *2*, 1358–1362. https://doi.org/10.1021/cs300219j.
44. Manolova, M., Böck, R., Scharf, I., Mehner, T., and Lampke, T. (2021). Electrodeposition of Pd alloys from choline chloride/urea deep eutectic solvents. J. Alloys Compd. *855*, 157462. https://doi.org/10.1016/j.jallcom.2020.157462.
45. Bernasconi, R., Panzeri, G., Accogli, A., Liberale, F., Nobili, L., and Magagnin, L. (2017). Electrodeposition from Deep Eutectic Solvents. Progress and Developments in Ionic Liquids. https://doi.org/10.5772/64935.
46. Protsenko, V.S., and Danilov, F.I. (2020). Current Trends in Electrodeposition of Electrocatalytic Coatings. In Methods for Electrocatalysis, Chams, A., A. Inamuddin, and Boddula R., eds. (Springer).
47. Plaza-Mayoral, E., Pereira, I.J., Nicole Dalby, K., Jensen, K.D., Chorkendorff, I., Falsig, H., Sebastián-Pascual, P., and Escudero-Escribano, M. (2022). Pd-Au Nanostructured Electrocatalysts with Tunable Compositions for Formic Acid Oxidation. ACS Appl. Energy Mater. *5*, 10632–10644. https://doi.org/10.1021/acsaem.2c01361.
48. Sebastián, P., Torralba, E., Vallés, E., Molina, A., and Gómez, E. (2015). Advances in Copper Electrodeposition in Chloride Excess. A Theoretical and Experimental Approach. Electrochim. Acta *164*, 187–195. https://doi.org/10.1016/j.electacta.2015.02.206.
49. Sebastián, P., Vallés, E., and Gómez, E. (2013). First stages of silver electrodeposition in a deep eutectic solvent. Comparative behavior in aqueous medium. Electrochim. Acta *112*, 149–158. https://doi.org/10.1016/j.electacta.2013.08.144.
50. Sebastián, P., Climent, V., and Feliu, J.M. (2018). Ionic Liquids in the Field of Metal Electrodeposition. Surface Science and Electrochemistry. https://doi.org/10.1016/B978-0-12-409547-2.13379-7.
51. El Abedin, S.Z., Pölleth, M., Meiss, S.A., Janek, J., and Endres, F. (2007). Ionic liquids as green electrolytes for the electrodeposition of nanomaterials. Green Chem. *9*, 549–555. https://doi.org/10.1039/b614520e.
52. Plaza-Mayoral, E., Dalby, K.N., Falsig, H., Chorkendorff, I., Sebastián-Pascual, P., and Escudero-Escribano, M. (2024). Preparation of Tunable Cu−Ag Nanostructures by Electrodeposition in a Deep Eutectic Solvent. Chemelectrochem, e202400094. https://doi.org/10.1002/celc.202400094.
53. Trasatti, S., and Petrii, O.A. (1992). Real surface area measurements in electrochemistry. J. electroanal. chem *327*, 353–376. https://doi.org/10.1016/0022-0728(92)80162-W.
54. Bard, A.J., and Faulkner, L.R. (2001). Electrochemical methods : fundamentals and applications. Potentials and Thermodynamics of Cells (Wiley Book), pp. 44–86.
55. Dollimore, D., Spooner, P., and Turner, A. (1976). The bet method of analysis of gas adsorption data and its relevance to the calculation of surface areas. Surf. Technol. *4*, 121–160. https://doi.org/10.1016/0376-4583(76)90024-8.
56. Plaza-Mayoral, E., Sebastián-Pascual, P., Dalby, K.N., Jensen, K.D., Chorkendorff, I., Falsig, H., and Escudero-Escribano, M. (2021). Preparation of high surface area Cu-Au bimetallic nanostructured materials by co-electrodeposition in a deep eutectic solvent. Electrochim. Acta *398*, 139309. https://doi.org/10.1016/j.electacta.2021.139309.
57. Sebastián-Pascual, P., and Escudero-Escribano, M. (2021). Surface characterization of copper electrocatalysts by lead underpotential deposition. J. Electroanal. Chem. *896*. https://doi.org/10.1016/j.jelechem.2021.115446.
58. Herrero, E., Buller, L.J., and Abruña, H.D. (2001). Underpotential deposition at single crystal surfaces of Au, Pt, Ag and other materials. Chem. Rev. *101*, 1897–1930. https://doi.org/10.1021/cr9600363.
59. Sebastián, P., Vallés, E., and Gómez, E. (2014). Copper electrodeposition in a deep eutectic solvent. First stages analysis considering Cu(I) stabilization in chloride media. Electrochim. Acta *123*, 285–295. https://doi.org/10.1016/j.electacta.2014.01.062.
60. NIST NIST Inorganic Crystal Structure Database (ICSD) SRD 3. https://icsd.nist.gov/.
61. Rumble, J.R., Bickham, D.M., and Powell, C.J. (1992). The NIST x-ray photoelectron spectroscopy database. Surf. Interface Anal. *19*, 241–246. https://doi.org/10.1002/sia.740190147.
62. Pauly, N., Tougaard, S., and Yubero, F. (2014). Determination of the Cu 2p primary excitation spectra for Cu, Cu 2O and CuO. Surf. Sci. *620*, 17–22. https://doi.org/10.1016/j.susc.2013.10.009.
63. Tahir, D., and Tougaard, S. (2012). Electronic and optical properties of Cu, CuO and Cu 2O studied by electron spectroscopy. J. Phys. Condens. Matter *24*, 175002. https://doi.org/10.1088/0953-8984/24/17/175002.
64. Pauly, N., Yubero, F., and Tougaard, S. (2016). Quantitative analysis of satellite structures in XPS spectra of gold and silver. Appl. Surf. Sci. *383*, 317–323. https://doi.org/10.1016/j.apsusc.2016.03.185.
65. Leiro, J., Minni, E., and Suoninen, E. (1983). Study of Plasmon Structure in XPS Spectra of Silver and Gold. J. Phys. F: Met. Phys. *13*, 215. https://doi.org/10.1088/0305-4608/13/1/024.
66. Liao, H., Fisher, A., and Xu, Z.J. (2015). Surface Segregation in Bimetallic Nanoparticles: A Critical Issue in Electrocatalyst Engineering (Preprint at Wiley-VCH Verlag). https://doi.org/10.1002/smll.201403380.
67. Hochfilzer, D., Sørensen, J.E., Clark, E.L., Scott, S.B., Chorkendorff, I., and Kibsgaard, J. (2021). The Importance of Potential Control for Accurate Studies of Electrochemical CO Reduction. ACS Energy Lett. *6*, 1879–1885. https://doi.org/10.1021/acsenergylett.1c00496.
68. Vavra, J., Shen, T.H., Stoian, D., Tileli, V., and Buonsanti, R. (2021). Real-time Monitoring Reveals Dissolution/Redeposition Mechanism in Copper Nanocatalysts during the Initial Stages of the CO2 Reduction Reaction. Angew. Chem. Int. Ed. Engl. *60*, 1347–1354. https://doi.org/10.1002/anie.202011137.
69. Trasatti, S., and Petrii, O.A. (1992). Real surface area measurements in electrochemistry. J. electroanal. chem *327*, 353–376. https://doi.org/10.1016/0926-860X(96)80148-7.
70. Li, D., Batchelor-McAuley, C., and Compton, R.G. (2020). Some thoughts about reporting the electrocatalytic performance of nanomaterials. Appl. Mater. Today *18*, 100404–100406. https://doi.org/10.1016/j.apmt.2019.05.011.
71. Zhang, H., Chang, X., Chen, J.G., Goddard, W.A., Xu, B., Cheng, M.J., and Lu, Q. (2019). Computational and experimental demonstrations of one-pot tandem catalysis for electrochemical carbon dioxide reduction to methane. Nat. Commun. *10*, 3340. https://doi.org/10.1038/s41467-019-11292-9.
72. Hori, Y., Murata, A., and Takahashi, R. (1989). Formation of hydrocarbons in the electrochemical reduction of carbon dioxide at a copper electrode in aqueous solution. Journal of the Chemical Society, Faraday Transactions 1. J. Chem. Soc., Faraday Trans. 1 *85*, 2309–2326. https://doi.org/10.1039/F19898502309.
73. Arán-Ais, R.M., Rizo, R., Grosse, P., Algara-Siller, G., Dembélé, K., Plodinec, M., Lunkenbein, T., Chee, S.W., and Roldan Cuenya, B. (2020). Imaging electrochemically synthesized Cu2O cubes and their morphological evolution under conditions relevant to CO2 electroreduction. Nat. Commun. *11*, 3489. https://doi.org/10.1038/s41467-020-17220-6.
74. Kratzer, P., Hammer, B., and Norskov, J.K. (1996). Geometric and Electronic Factors Determining the Differences in Reactivity of H2 on Cu(100) and Cu(111).Surface. Science. https://doi.org/10.1016/0039-6028(96)00309-3.
75. Reske, R., Mistry, H., Behafarid, F., Roldan Cuenya, B., and Strasser, P. (2014). Particle size effects in the catalytic electroreduction of CO2 on Cu nanoparticles. J. Am. Chem. Soc. *136*, 6978–6986. https://doi.org/10.1021/ja500328k.
76. Quan, Y., Zhu, J., and Zheng, G. (2021). Electrocatalytic Reactions for Converting CO 2 to Value-Added Products. Small Science *1*, 2100043. https://doi.org/10.1002/smsc.202100043.
77. Popović, S., Smiljanić, M., Jovanovič, P., Vavra, J., Buonsanti, R., and Hodnik, N. (2020). Stability and Degradation Mechanisms of Copper-Based Catalysts for Electrochemical CO2 Reduction (Preprint at Wiley-VCH Verlag). https://doi.org/10.1002/anie.202000617.
78. Huang, J., Hörmann, N., Oveisi, E., Loiudice, A., De Gregorio, G.L., Andreussi, O., Marzari, N., and Buonsanti, R. (2018). Potential-induced nanoclustering of metallic catalysts during electrochemical CO2 reduction. Nat. Commun. *9*, 3117. https://doi.org/10.1038/s41467-018-05544-3.
79. Arán-Ais, R.M., Gao, D., and Roldan Cuenya, B. (2018). Structure- and Electrolyte-Sensitivity in CO2 Electroreduction. Acc. Chem. Res. *51*, 2906–2917. https://doi.org/10.1021/acs.accounts.8b00360.
80. Kortlever, R., Shen, J., Schouten, J.P., Calle-Vallejo, F., and Koper, M.T.M. (2015).

Catalysts and Reaction Pathways for the Electrochemical Reduction of Carbon Dioxide. J. Phys. Chem. Lett. https://doi.org/10.1021/acs.jpclett.5b01559.

81. Schouten, K.J.P., Kwon, Y., Van Der Ham, C.J.M., Qin, Z., and Koper, M.T.M. (2011). A new mechanism for the selectivity to C1 and C2 species in the electrochemical reduction of carbon dioxide on copper electrodes. Chem. Sci. *2*, 1902–1909. https://doi.org/10.1039/c1sc00277e.
82. Zheng, Y., Vasileff, A., Zhou, X., Jiao, Y., Jaroniec, M., and Qiao, S.Z. (2019). Understanding the Roadmap for Electrochemical Reduction of CO2 to Multi-Carbon Oxygenates and Hydrocarbons on Copper-Based Catalysts. J. Am. Chem. Soc. *141*, 7646–7659. https://doi.org/10.1021/jacs.9b02124.
83. Li, J., Xiong, H., Liu, X., Wu, D., Su, D., Xu, B., and Lu, Q. (2023). Weak CO binding sites induced by Cu–Ag interfaces promote CO electroreduction to multi-carbon liquid products. Nat. Commun. *14*, 698. https://doi.org/10.1038/s41467-023-36411-5.
84. Nguyen, T.N., and Dinh, C.T. (2020). Gas diffusion electrode design for electrochemical carbon dioxide reduction. Preprint at Royal Society of Chemistry *49*, 7488–7504. https://doi.org/10.1039/d0cs00230e.
85. Burdyny, T., and Smith, W.A. (2019). CO2 reduction on gas-diffusion electrodes and why catalytic performance must be assessed at commercially-relevant conditions. Energy Environ. Sci. *12*, 1442–1453. https://doi.org/10.1039/c8ee03134g.
86. Wakerley, D., Lamaison, S., Wicks, J., Clemens, A., Feaster, J., Corral, D., Jaffer, S.A., Sarkar, A., Fontecave, M., Duoss, E.B., et al. (2022). Gas diffusion electrodes, reactor designs and key metrics of low-temperature CO2 electrolysers. Nat. Energy *7*, 130–143. https://doi.org/10.1038/s41560-021-00973-9.

STAR★METHODS

KEY RESOURCES TABLE

REAGENT OR RESOURCE	SOURCE	IDENTIFIER
Software and algorithms		
VESTA software package	JP-Minerals	https://jpminerals.org/vesta/en/
OriginPro2023	OriginLab	https://www.originlab.com/; RRID:SCR_002815
Avantage Data System	Thermofisher	https://www.thermofisher.com/order/catalog/product/IQLAADGACKFAKRMAVI; RRID:SCR_008452

RESOURCE AVAILABILITY

Lead contact

Further information and requests for resources should be directed to and will be fulfilled by the lead contact, María Escudero-Escribano (maria.escudero@icn2.cat).

Materials availability

The study did not generate new unique materials.

Data and code availability

Data: All data reported in this paper will be shared by the lead contact upon request.
Code: This paper does not report the original code.
Any additional information required to reanalyze the data reported in this paper is available from the lead contact upon request.

EXPERIMENTAL MODEL AND STUDY PARTICIPANTS DETAILS

There are no experimental models (animals, human subjects, plants, microbe strains, cell lines, primary cell cultures) used in the study.

METHOD DETAILS

Preparation of the nanostructured Cu-Ag deposits from DES

The metal salts $CuCl_2$ (Sigma-Aldrich, 99%) and AgCl (Sigma-Aldrich, 99%) were dissolved in a 1:2 choline chloride (ChCl, Acros Organics, 99%) and urea (Sigma-Aldrich, 99%) DES under magnetic stirring at 60°C. Three different baths were prepared for the electrodeposition of the metallic nanostructures: (a) 0.075 M $CuCl_2$ / 0.025 M AgCl + DES solution, corresponding to 3Cu:1Ag molar ratio solution; (b) 0.086 M $CuCl_2$ / 0.014 AgCl + DES solution, corresponding to 6Cu:1Ag molar ratio solution; (c) 0.1 M $CuCl_2$ + DES solution. Prior to the electrodeposition, the bath solutions were dried with a N_2 or Ar stream for several hours to avoid the solvent co-reduction and reduce the quantity of water on the solvent, facilitating the deposition.

We performed the electrodeposition process by applying a constant potential until we reached a specific charge by chronoamperometry on a thermostatic three-electrode glass cell with a PTFE cap as shown in Figure S1 of the Supplementary Information (S.I). The counter electrode for the Cu-Ag baths was a Pt wire, while we used a Ag wire as pseudo reference electrode. Both were pre-treated by flame-annealing and rising with ultrapure water (Sartorius Arium Pro). When necessary, a 10 % diluted HNO_3 solution (Sigma-Aldrich) was used to remove metallic traces. For the single Cu solution in DES, copper wires were used both as counter and pseudo reference electrodes. Here, they were pre-treated with a 10 % diluted HNO_3 solution and rinsed abundantly with ultrapure water. The working electrodes (WE) were Glassy Carbon (GC) plates of 25*25 mm^2 and 3 mm thickness, one side diamond polished to mirror finish (SIGRADUR G plates, HTW GmbH). All potential values were referenced against the Ag|AgCl scale. Right before the electrodeposition, the GC electrodes were prepared by polishing with water-based α-alumina powder of 0.3 and 0.05 μm coarseness (Struers). Subsequently, they were rinsed and sonicated with ultrapure water to remove all alumina traces and dried with N_2 stream. The temperature of the DES baths was always kept at 70°C with a water bath to reduce the viscosity increasing the deposition rates and avoiding the solvent co-reduction.[59] We have analyzed the co-electrodeposition of the two bath solutions used for CO_2RR in this study: 3Cu:1Ag and 6Cu:1Ag molar ratio solutions using cyclic voltammetry (CV) and chronoamperometry (CA). For the measurements and analysis, we used a NOVA potentiostat and software.

We have used two different sizes and shapes of glassy carbon (GC) electrodes for all electrochemical characterization. The GC plate of 2.5x2.5 cm^2 (where the electrodeposition was performed in an area of 2.3x2.3 cm^2) used throughout all the manuscript, and a small GC rod of 5 mm of diameter. The three-electrode cells used for both GC are shown in Figure S1. We prove that the Cu and Cu-Ag

electrodeposition is scalable to a bigger glassy carbon such as the 2.3x2.3 cm^2 used as the working electrode for the CO_2RR. The results obtained in the 2.3x2.3 cm^2 glassy carbon and in a glassy carbon rod with 0.196 cm^2 of area are consistent between them. For simplicity and for the advantage of working with the electrode under meniscus configuration, we have recorded the CVs and CAs of the electrodeposition process in the small three-electrode cell with the glassy carbon rod. This configuration is used to record the CVs of the deposition process more precisely since only the polished surface of the glassy carbon is in contact with the solution.

CO_2 electroreduction (CO_2RR) measurements and analysis

The electrochemical reduction of CO_2 was evaluated at ambient pressure CO_2 in a customized polycarbonate H-cell fitted with Buna-N O-rings. The chosen electrolyte was a 0.1 M $KHCO_3$ obtained by bubbling CO_2 (Carbagas, 99.999%) through 0.05 M K_2CO_3 (Acros Organics, 99+ %,) solution for 1 h. Each measurement was analyzed using a Biologic SP-300 potentiostat in a chronoamperometry regime for one hour at applied potentials between -0.8 V_{RHE} and -1.3 V_{RHE}. Three separate measurements of each sample prepared on different days were tested at each applied potential. The represented data is the average values of the three measurements. We calculated the ohmic drop at each sample by electrochemical impedance spectroscopy (EIS) and corrected the chronoamperometry potential following the equation $E = E_{ap} - iR_{\Omega}$. The reference electrode was a Ag|AgCl electrode (Innovative Instruments, Inc) which was tested against the master electrode prior to the measurements, and the measured voltages were then converted to the reversible hydrogen electrode scale (RHE). The working electrodes were the electrodeposited Cu and CuAg nanostructures on the GC electrodes. The geometric area in contact with the solution was 1.39 cm^2. The counter electrode was a Pt foil pre-treated by flame-annealing and rinsing with ultrapure water. Both working and counter electrode were positioned in parallel to allow uniform potential distribution. The anion exchange membrane separating the catholyte from the anolyte was a Selemion AMVN. Each compartment was filled with 2 mL of electrolyte solution. During reaction, the electrolyte of both compartments was constantly bubbled with CO_2 at a flow of 5 sccm to keep the solution saturated with CO_2, ensure that CO_2 reaches the electrode surface, and allow a continuous analysis of the gas products through the on-line gas chromatograph. The gas products were detected by the SRI 8610C gas chromatograph (GC) with a HayeSep D porous polymer column, thermal conductivity detector, flame ionization detector and, nitrogen (99.999 %) as the carrier gas. Then, the calibration curves from standard gas mixtures were employed to calculate the concentration of each gas product. The liquid products were analyzed by high-performance liquid chromatography (HPLC) on a Thermo Scientific UltiMate 3000 instrument. The eluent for the HPLC analysis was a 5 mM H_2SO_4 solution.

Determination of faradic efficiencies and partial currents of the CO_2RR products on different Cu and Cu-Ag nanostructures

The partial current densities are normalized by the ECSA and R calculated from the lead UPD on each sample. Since $R = A_{ECSA}/A_{G_{EO}}$, the total currents obtained from the measurements are first divided by the geometric area in contact with the CO_2RR electrolyte and subsequently divided by the roughness factor obtained from the lead UPD:

$$j_{GA}\left(mA\ cm^{-2}\right) = i\,(mA) \,/\, A_{GEO}\left(cm^2\right)$$

$$j_{ECSA}\left(mA\ cm^{-2}\right) = j_{GA}\left(mA\ cm^{-2}\right) \,/\, R$$

Where i (mA) is the recorded total current from the CO_2RR experiment, A_{GEO} (cm^2) is the geometric area where the CO_2RR is taking place, j_{GA} (mA cm^2) is the total current density normalized by the geometric area, R is the roughness factor estimated from the lead UPD experiments (values from Table S1) and j_{ECSA} (mA cm^{-2}) is the total current density normalized by the ECSA.

From the total current densities normalized by the ECSA (i.e., intrinsic current densities), we proportionally calculated the intrinsic partial current densities from the partial FEs (%) of each of the detected products as follows:

$$j_{ECSA}^{product}\left(mA\ cm^{-2}\right) = \frac{FE_{product}(\%)\cdot j_{ECSA}\left(mA\ cm^{-2}\right)}{100}$$

where $j_{ECSA}^{product}\left(mA\ cm^{-2}\right)$ is the partial current density of an specific product normalized by the ECSA, $FE_{product}$ (%) is the partial faradaic efficiency associated to that product, and $j_{ECSA}\left(mA\ cm^{-2}\right)$ is the total current density normalized by the ECSA.

Pb underpotential deposition (UPD) and estimation of the ECSA and roughness factor (R)

The Pb-UPD measurements were carried out on a three-electrode cell like the one used for the electrodeposition. We used a solution of 2 mM $Pb(ClO_4)_2$ (Sigma-Aldrich, ≥ 99.995 %) + 0.1 M $KClO_4$ (Sigma-Aldrich, ≥ 99.99 %) + 1 mM $HClO_4$ (suprapur 70 %, Merck) in milli-Q (18.2 MΩcm, TOC < 5 ppm) water. The counter and reference electrodes were the same as for the electrodeposition experiments. The working electrodes were our deposited Cu and Cu-Ag nanostructures on the GC. UPD is a surface process sensitive to the structure and real area of the catalysts. By integrating the involved charges of the anodic and cathodic voltammetric scans of the Pb UPD cyclic voltammograms (CVs), we can estimate the ECSA and roughness factor (R) of our nanostructures. An average from the anodic and cathodic integrated charges is used for the calculations since UPD is a reversible process. Those values were used to determine the ECSA and R of our nanostructures using the following equation:

$$ECSA = Q(\mu C) Q_0^{CuAg}\left(\mu C\ cm^{-2}\right)$$

$$R = A_{ECSA}(cm^2)/A_{GEO}(cm^2)$$

Where Q is the average integrated charge, $Q_0^{Cu,Ag}$ is the average of the surface charge density values of the lead UPD on polycrystalline extended Cu and Ag surfaces, A_{ECSA} is the calculated electrochemically active surface area and A_{GEO} is the geometric area of our electrode.

Determination of the mass loading of Cu and Cu-Ag

We have fixed the deposition circulated charge to -200 mC, -270 mC and -485 mC to control the amount of deposited Cu and Cu-Ag in each electrode. We have analyzed the molar ratios and atomic ratios of Cu and Ag from the compositional analysis of the EDS and the XPS. Together with the Faraday law, we have determined the loading of each deposit. To avoid overestimation of the loadings, we have assumed a 100% percent of deposition efficiency. Equation 1 contains the Faraday law:

$$Q = znF \quad (1)$$

Q is the circulated charge (in mC), *F* is the Faraday constant (in 96500 C/mol e^-), *n* is the number of moles of deposited metal (mol M) and *z* is the number of transferred electrons per metal atom (mol e-/mol M). From the $CuCl_2$ and AgCl salts employed, we consider the following reactions:

$$Cu^{2+} + 2e- \rightarrow Cu,\ z_{Cu} = 2 \quad (2)$$

$$Ag^{1+} + 1e- \rightarrow Ag,\ z_{Ag} = 1 \quad (3)$$

The EDS and XPS measurements have provided the molar ratio Cu/Ag:

$$\frac{m\ Cu}{p\ Ag} \quad (4)$$

Total moles of Cu are *m*n* and the total moles of Ag are *p*n*. Taking into account the atomic mass of each metal MCu and MAg (g/mol) and based on these equations, we have calculated the loadings of Cu and Ag of each deposit as follows:

$$\text{loading Cu} - \text{Ag} = \frac{Q}{F} * \frac{(MCu * m) + (MAg * p)}{(2 * m) + (1 * p)} \quad (5)$$

Morphological and compositional analysis

Three different scanning electron microscopes (SEM) were used for the morphological analysis of our nanostructures before and after reaction. A JEOL 7800-F prime SEM housed at the Niels Bohr Institute at the University of Copenhagen, a high-resolution Zeiss Gemini 500 field-emission scanning electron microscope (FE-SEM) at Topsoe S/A, and a Thermo-Fisher Teneo using an in-lens (Trinity) detector at Ecole Polytechnique Fédérale de Lausanne (EPFL). The first two microscopes were used to acquire the images with a beam energy of 2 kV while the third used 5 kV.

The energy-dispersive X-Ray spectroscopy (EDS) analysis was carried out on two different microscopes using two different EDS detectors. A Thermo Scientific UltraDry silicon drift detector with Pathfinder Software was used for the EDS acquired from Topsoe, and a Bruker XFlash Silicon drift EDX detector with Esprit software was used for the EDS analysis performed at EPFL. In both cases, accelerating voltage of 15 kV was used to collect the EDS data.

For a more insightful surface composition analysis, X-ray Photoelectron spectroscopy (XPS) was performed at the Technical University of Denmark (DTU) by a Theta Probe instrument (Thermo Scientific) using an Al anode X-ray source (Kα line = 1486.6 eV). The XPS chamber's base pressure was < 5.0 $\times 10^{-8}$ mbar. All measurements used a X-ray beam size of 400 μm and a pass energy of 100 eV. Each survey recorded 20 scans while each element spectra recorded 50 scans. We carried out a depth analysis by sputtering (4 kV and 1.0 μA) with N6 Ar (1.1 $\times$ 10^{-7} mbar) the samples for 40 seconds, 20 seconds per level. The spectra were recorded on each level, where level 0 means no sputtering. After the survey scans, C1*s*, O1*s*, Cu2*p*, and Ag3*d* peaks were measured in steps of 0.1 eV. We used Thermo Avantage Software for the data acquisition and analysis with a Shirley type background for all instances.

The surveys and spectra of every peak have been recorded before and after sputtering. Figure S6A and Figure S6B show the surveys of the 3Cu:1Ag and 6Cu:1Ag, respectively. We have noted a shift (observed with the dashed grey line) in the binding energies of the level 0 survey from the sample of 3Cu:1Ag (Figure S6A). After the first sputtering, all peaks were placed close to their tabulated values. We observed the Carbon 1s peak centered at 284.8 eV.6,7 Regarding the Cu2p and 3d peaks, they become intensified with sputtering. The surveys from level 1 and level 2 are mainly equal, suggesting that all traces of contamination have been removed already after 20 seconds of sputtering. We have recognized the same peaks for the 6Cu:1Ag sample and no shift is observed in any of the levels. For this reason, we only show the Cu2p and

Ag3d spectrum analysis of the 3Cu:1Ag and 6Cu:1Ag after 20 seconds of sputtering (level 1) in Figure S7. We have used the GC rod of 5 mm for the XPS analysis in order to employ an adaptable sample which properly fits with the holder of our XPS equipment.

QUANTIFICATION AND STATISTICAL ANALYSIS

Standard deviations and errors of at least three independent measurements were calculated using Microsoft Excel.

ADDITIONAL RESOURCES

Our study has not generated or contributed to a new website/forum or has not been part of a clinical trial.